Sustainable Energy & Fuels

Interdisciplinary research for the development of sustainable energy technologies

Accepted Manuscript

This article can be cited before page numbers have been issued, to do this please use: D. Wu, H. Yan, X. Zhao, Y. Qiu, Y. Yang, Y. Zhang, B. Fan, P. Cui, X. Sun, P. Zhao and M. Li, *Sustainable Energy Fuels*, 2025, DOI: 10.1039/D5SE00128E.

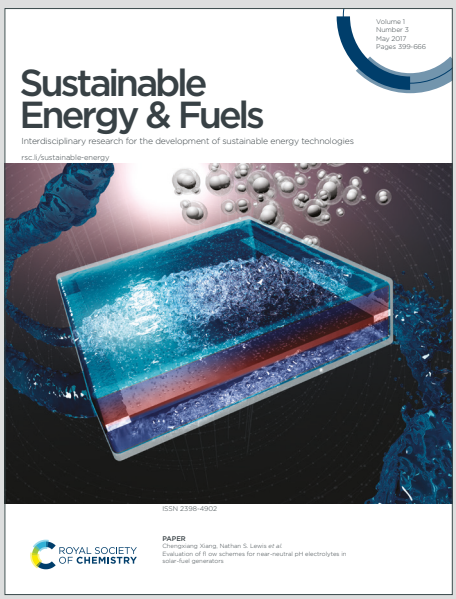

ROYAL SOCIETY OF CHEMISTRY

rsc.li/sustainable-energy

View Article Online
DOI: 10.1039/D5SE00128E

ARTICLE

Enhanced SnO_2 Electron Transport Layer by Eu^{3+} for Efficient and Stable Perovskite Solar Cells

Received 00th January 20xx,
Accepted 00th January 20xx

DOI: 10.1039/x0xx00000x

Danxia Wu,[a] Huilin Yan,[a] Xing Zhao,*[a] Yujie Qiu,[a] Yuqing Yang,[a] Yuanxi Zhang,[a] Bingbing Fan,[a] Peng Cui,[a] Xin Sun,[a] Pengjun Zhao [b] and Meicheng Li *[a]

Chemical bath deposition (CBD) is a promising way to fabricate SnO_2 electron transport layers (ETLs) in efficient and stable perovskite solar cells (PSCs). Here, europium chloride hexahydrate ($EuCl_3{\cdot}6H_2O$) was introduced into the CBD process to optimize the properties of SnO_2 for high-efficiency and stable PSCs. The incorporation of Eu^{3+} ions into the SnO_2 lattice effectively enhances its electrical properties, mitigates surface trap defects, and reduces interfacial non-radiative recombination. More importantly, Eu^{3+} ions serve as effective protectants, improving the UV resistance of perovskite films. As a result, the PSCs based on Eu-SnO_2 ETL exhibit a notable improvement in power conversion efficiency (PCE), increasing from 22.02% to 24.50%. Additionally, the devices demonstrate excellent stability, maintaining 96.9% and 86% of their initial efficiency after 2600 h in ambient air and 130 h under continuous UV illumination, respectively. This strategy provides a valuable approach for further improving the film quality of SnO_2, offering great potential for high-efficiency and stable PSCs.

Introduction

After more than a decade of development, perovskite solar cells (PSCs) have achieved a certified photovoltaic conversion efficiency (PCE) exceeding 26%, establishing them as the leading technology among emerging photovoltaics.[1–3] In conventional n-i-p structured PSCs, electron transport layers (ETLs) are critical to their photovoltaic performance, as they not only collect and transport electrons but also influence the crystal growth of perovskite films.[4] Compared to TiO_2, SnO_2 offers superior chemical stability, higher electron mobility, well-matched band alignment, and compatibility with low-temperature processing, making it a promising ETL for industrial commercialization.[5]

The SnO_2 ETL can be prepared whether by spin-coating of colloidal precursor solutions or chemical bath deposition (CBD).[6,7] Even though the CBD technique can achieve a more uniform and dense SnO_2 layer, enabling a high open-circuit voltage (V_{OC}) of up to 1.2 V.[8] However, surface defects, such as hydroxyl groups, commonly form on the SnO_2 surface, reducing device efficiency and accelerating perovskite decomposition at the bottom interface.[9] These imperfections hinder electron transport and exacerbate instability under operational conditions, posing a critical challenge to long-term device performance.[10] Surface passivation with external species is a promising way to decrease detrimental surface oxygen defects, such as alkali salts,[11] halogens,[12] organic acids,[13] and H_2O_2.[14] These chemicals effectively reduce surface trap defects and non-radiative recombination, improving interfacial contact and enhancing the photovoltaic performance of PSCs. Moreover, under light soaking, high-energy UV light primarily impacts the bottom surface of the perovskite, reducing Pb^{2+} to Pb^0 and damaging device efficiency and stability.[15] Lanthanide materials can facilitate down-conversion and mitigate UV light exposure.[16,17] Additionally, Eu^{3+} ions can oxidize the deep-level trap defects, converting Pb^0 into Pb^{2+}.[18] Lanthanides also enhance the crystallinity of perovskite films, thereby enhancing the photovoltaic performance of PSCs.[19] Given these advantages, Eu^{3+} ions are promising candidates for optimizing the buried interface of PSCs. Although Eu^{3+} ions exhibit a passivation effect at buried interface,[20] a more in-depth investigation into their impact on the properties of SnO_2 is essential for achieving high-quality CBD-SnO_2 and high-efficiency PSCs.

In this study, we optimized the SnO_2 ETL by introducing europium chloride hexahydrate ($EuCl_3{\cdot}6H_2O$) during the CBD process. GIXRD analysis confirms the successful incorporation of Eu^{3+} ions into the SnO_2 lattice. XPS analysis shows that the Eu^{3+} promotes the formation of Sn^{4+} and decreases the traps defects at SnO_2 surface. Furthermore, both electrical and electron mobility are improved after Eu doping. These improvements boosted charge collection and charge transportation efficiency, leading to significant gains in device efficiency and stability. As a result, the efficiency of PSCs increased from 22.02% to 24.50% after Eu doping. The Eu-treated PSC also demonstrated good stability, retaining 96.9% of its initial efficiency after 2600 hours in ambient air.

[a.] State Key Laboratory of Alternate Electrical Power System with Renewable Energy Sources, School of New Energy, North China Electric Power University, Beijing 102206, China
[b.] State Key Laboratory of Functional Materials and Devices for Special Environmental Conditions, Xinjiang Key Laboratory of Electronic Information Materials and Devices, Xinjiang Technical Institute of Physics and Chemistry of Chinese Academy of Sciences, Urumqi 830011, China

Supplementary Information available: [details of any supplementary information available should be included here]. See DOI: 10.1039/x0xx00000x

View Article Online
DOI: 10.1039/D5SE01285

Results and Discussion

In this work, SnO_2 ETLs were prepared using the CBD technique according to a published report.[21] 0.14 mM $EuCl_3{\cdot}6H_2O$ was added to the precursor solution as a dopant to regulate SnO_2 crystal growth (0.14 mM is the optimal concentration for device photovoltaic performance, as discussed in the following section). The ETLs with or without Eu doping are referred to as Eu-SnO_2 and SnO_2, respectively. X-ray photoelectron spectroscopy (XPS) was performed to investigate the chemical states of the SnO_2 ETLs before and after Eu doping, as shown in Fig. 1a-e. The corresponding XPS survey spectra are presented in Fig. S1 (Supporting Information). In Fig. 1a, the Eu^{3+} $3d_{5/2}$ and Eu^{3+} $3d_{3/2}$ peaks appear at 1135.58 and 1165.98 eV, respectively, while no such peaks are observed in the undoped SnO_2, confirming the presence of Eu in the Eu-SnO_2 films. Fig. 1b presents the Eu 4d XPS spectra, where a singlet peak at 139.48 eV in SnO_2 corresponds to the Sn 4s peak. Upon Eu doping, a broad overlap of Eu 4d and Sn 4s peaks is observed, comprising three distinct peaks. The peaks at 136.87 and 142.88 eV correspond to the Eu^{3+} $4d_{5/2}$ and Eu^{3+} $4d_{3/2}$, respectively. Notably, a new peak at 128.26 eV appears for Eu-SnO_2, which can be attributed to the formation of Eu^{2+},[22] suggesting that Eu^{3+} was partially reduced to Eu^{2+} during the CBD process. Eu 3d and Eu 4d XPS spectra of heavily-doped Eu-SnO_2 (1.4 mM) are also present in Fig. S2 (Supporting Information) to confirm this result.

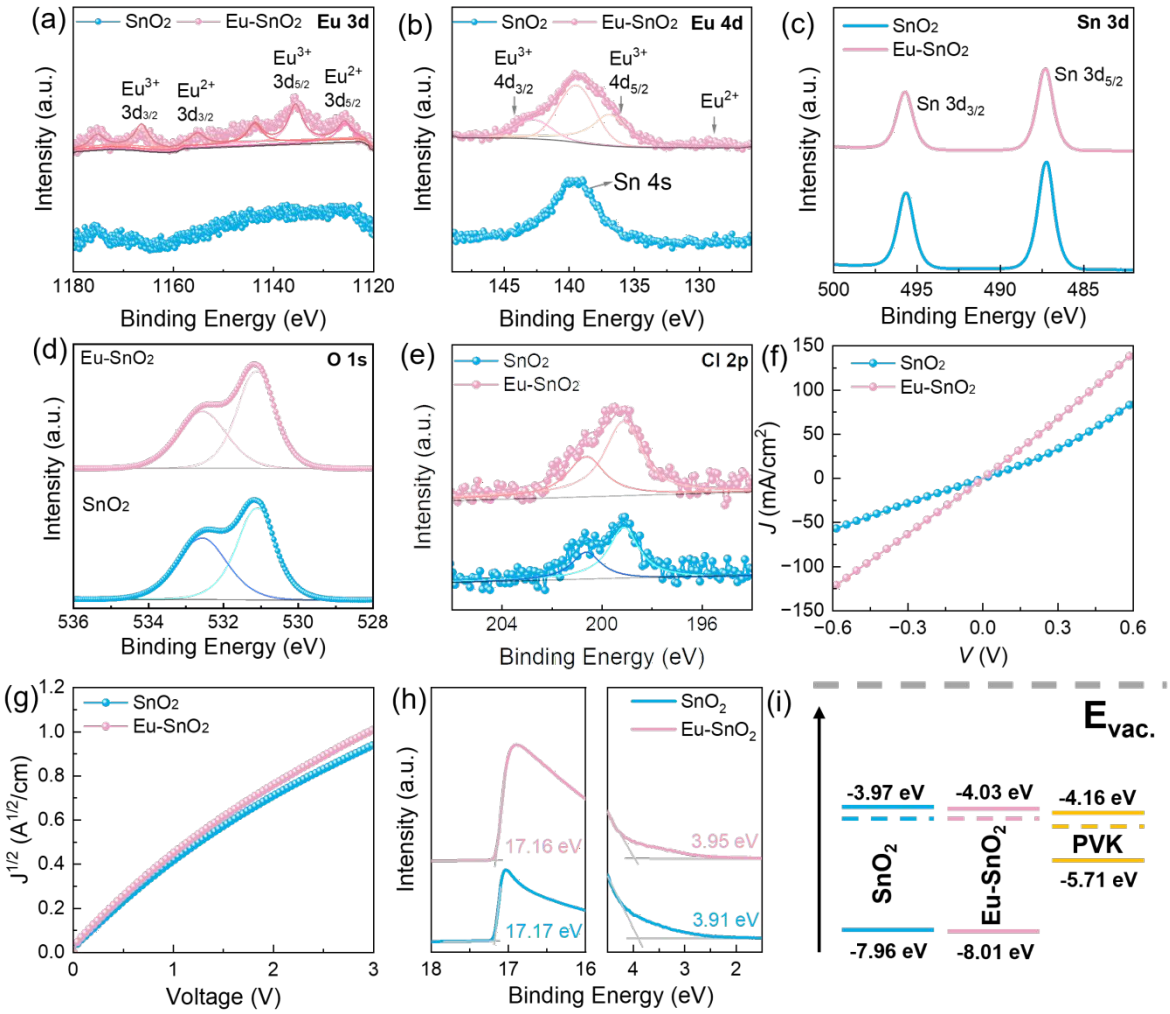

Fig. 1 Characterization of SnO_2 films. XPS spectra of SnO_2 and Eu-SnO_2: (a) Eu 3d, (b) Eu 4d, (c) Sn 3d, (d) O1s and (e) Cl 2p. (f) *J-V* curves of simi-devices with the structure FTO/SnO_2(or Eu-SnO_2)/Au. (g) Electron mobility characterization of electron-only semi-devices with the structure FTO/SnO_2(or Eu-SnO_2)/PCBM/Au. (h) UPS spectra and (f) Energy level diagram of ETL and perovskite films.

As shown in Fig. 1c, the Sn $3d_{3/2}$ and Sn $3d_{5/2}$ XPS peaks, initially observed at 487.2 and 495.6 eV for SnO_2, shifted to 487.3 and 495.7 eV after Eu doping, indicating electron loss from Sn atoms. For the O 1s spectra in Fig. 1d, the main peak at 531.2 eV represents lattice oxygen, while the shoulder peak at 532.5 eV represents hydroxyl oxygen (–OH) on the surface of SnO_2. By fitting and analysing the peak areas, the ratio of the shoulder peak area (S_{-OH}) to the total O1s spectral area (S_{all}) decreased from 46.6% to 42.9% after Eu doping. This reduction indicates that Eu incorporation effectively passivates –OH defects on the SnO_2 surface.[23] The introduction of $EuCl_3{\cdot}6H_2O$ also increased the Cl content, as shown in Fig. 1e, which can promote the crystallization of perovskite. To compare the electrical properties of SnO_2 ETLs before and after Eu doping, we

View Article Online
DOI: 10.1039/D5SE01625E

fabricated semi-devices with the structure FTO/SnO_2 (or Eu-SnO_2)/Au for conductivity testing and observed an improvement in conductivity with Eu doping, as shown in Fig. 1f. The resistance of the ETL film is inversely proportional to the slope of current-voltage (*J-V*) curves. An increased slope indicates a decreased resistance after Eu doping, mainly ascribed to the introduction of Eu^{3+}, which forms n-type doping on SnO_2. We also fabricated electron-only devices with the structure FTO/SnO_2 (or Eu-SnO_2)/PCBM/Au, and the *J-V* curves of these semi-devices are shown in Fig. 1g. Carrier mobility was determined using the Mott-Gurney law: $\mu=8JL^3/9\varepsilon\varepsilon_0V^2$, where *J* is the current density, L is the ETL thickness, ε is the relative dielectric constant of SnO_2, ε_0 is the vacuum permittivity, and *V* is the applied voltage. The calculated electron mobility of SnO_2 is 4.06×10^{-5} $cm^2/(V\cdot s)$, whereas Eu-SnO_2 exhibits a higher electron mobility of 4.35×10^{-5} $cm^2/(V\cdot s)$. Ultraviolet photoelectron spectroscopy (UPS) was performed to characterize the energy level changes of perovskite and ETL films. The UPS spectra and corresponding Tauc plots for different ETLs are presented in Fig. 1h and Fig. S3 (Supporting Information), with those for perovskite shown in Fig. S4 (Supporting Information). By fitting the UPS spectra and Tauc plots, we calculated the conduction and valence bands, and the resulting energy level diagram is shown in Fig. 1i. The introduction of Eu alters the energy level of SnO_2, reducing the energy barrier from 0.19 to 0.13 eV. The energy difference between the Fermi level and the conduction band decreased from 0.08 eV for SnO_2 to 0.03 eV for Eu-SnO_2, demonstrating that the incorporation of Eu induces n-type doping on SnO_2. The enhanced electrical properties and decreased energy barrier benefit the charge carrier transport in PSCs.

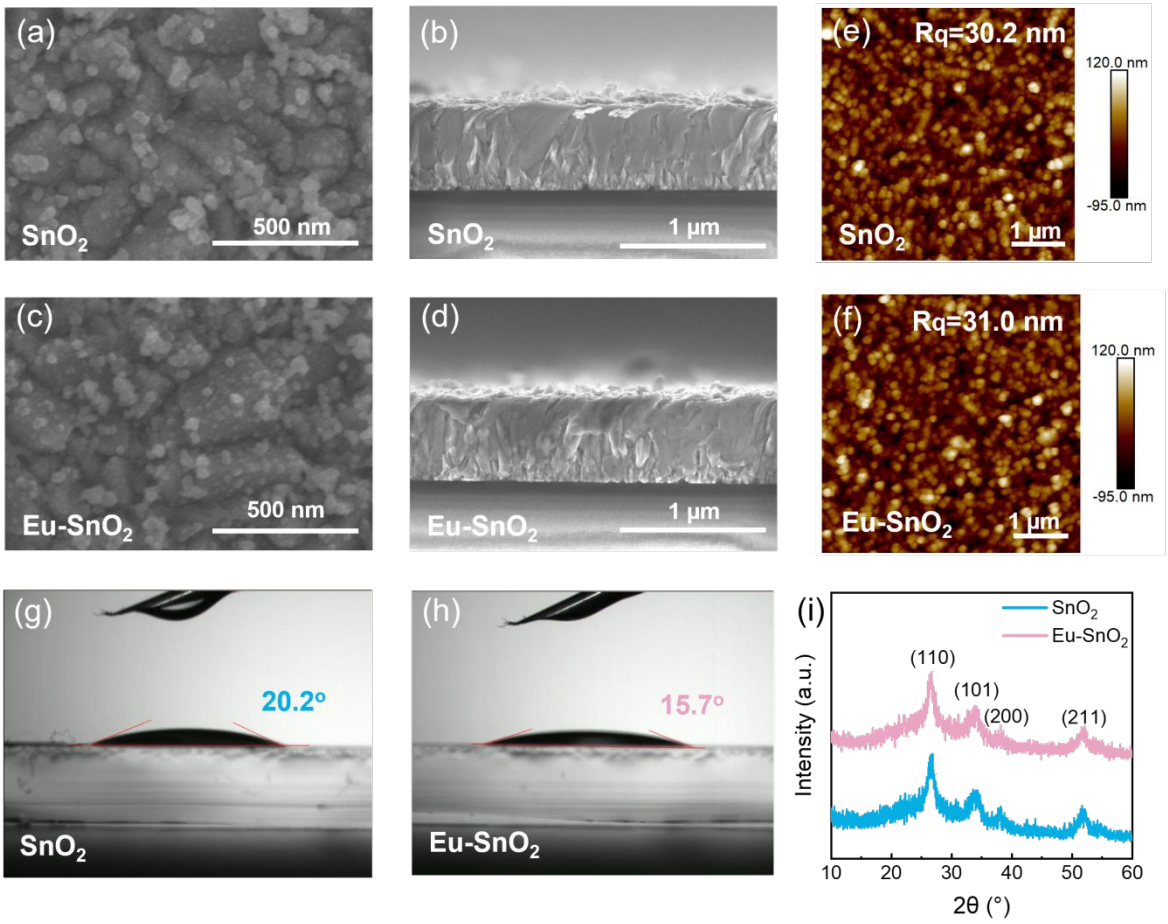

Fig. 2 (a) Top-view and (b) cross-sectional SEM images of SnO_2 film. (c) Top-view and (d) cross-sectional of Eu-SnO_2 film. (e, f) Surface roughness of SnO_2 and Eu-SnO_2 films. (g, h) Contact angles of PbI_2 solutions on SnO_2 and Eu-SnO_2 films. (i) GIXRD patterns of SnO_2 films with and without $EuCl_3\cdot6H_2O$.

The luminescence behaviour of Eu-SnO_2 has been investigated (Fig. S5a, Supporting Information), and the photoluminescence (PL) excitation bands are observed at ~280 nm, ~300 nm and ~360 nm. The emission spectra of Eu-SnO_2 have been monitored at 280 nm. As shown in Fig. S5b (Supporting Information), Eu-SnO_2 exhibits distinct emission peaks associated with Eu^{2+} 5d-4f transitions in the 350-500 nm range and Eu^{3+} $^5D_0$-^7F_J (J = 0,1 and 2) transitions in the 560-620 nm range.[24,25] In contrast, SnO_2 does not display such emission features. These results confirm that Eu ions in Eu-SnO_2 effectively facilitate down-conversion, converting high-energy photons into lower-energy emissions.

To evaluate the impact of Eu^{3+} ions on SnO_2 crystal growth, we performed the scanning electron microscopy (SEM) to check the morphologies of SnO_2 and Eu-SnO_2 ETLs, as shown in Fig. 2a-d. Top-view SEM images (Fig. 2a and 2c) reveal that both SnO_2 and Eu-SnO_2 form ultra-compact, dense films on FTO substrates, effectively preventing unwanted current leakage in devices.

View Article Online
DOI: 10.1039/D5SE00138E

Cross-sectional SEM images indicate a consistent thickness of approximately 70 nm for both ETLs. Unlike organic dopants,[26,27] which strong coordinate with Sn^{2+} ions and alter SnO_2 morphology, Eu^{3+} ions have minimal impact on the morphologies of SnO_2 ETLs. Atomic force microscopy (AFM) was used to measure the surface roughness of the ETLs, as shown in Fig. 2e and 2f. The root mean square (R_q) values are 30.2 nm for SnO_2 and 31.0 nm for Eu-SnO_2, indicating similar surface roughness, consistent with the SEM observations. Surface contact angles, shown in Fig. 2g and 2h, decreased from 20.2° for SnO_2 to 15.7° for Eu-SnO_2, demonstrating improved wettability, which facilitates better perovskite deposition. Grazing incidence X-ray diffraction (GIXRD) was performed to analyse the crystallinity of the SnO_2 films, as shown in Fig. 2i. Both ETLs exhibit diffraction peaks at the (110), (101), and (211) lattice planes, corresponding to the tetragonal rutile structure of SnO_2. The 2θ diffraction peak of the (110) plane shifted from 26.82° for SnO_2 to 26.72° for Eu-doped SnO_2, indicating lattice expansion due to the substitution of Sn^{4+} (0.69 Å) by the larger Eu^{3+} ions (0.947 Å). The full width half maximum (FWHM) and crystal size of the SnO_2 ETLs, summarized in Table S1 (Supporting Information), show that the FWHM of (110) lattice plane increases from 1.63° for SnO_2 to 1.66° for Eu-SnO_2, while the crystal size decreases from 4.95 to 4.85 nm. These changes suggest that Eu is successfully incorporated into the SnO_2 lattice.[28,29] To confirm this trend, heavily doped SnO_2 (1.4 mM) was also analysed, and the corresponding GIXRD pattern is shown in Fig. S6 (Supporting Information). The 2θ diffraction peak of the (110) plane shifted to 26.54°, with an FWHM and a crystal size measured at 1.83° and 4.12 nm, respectively. These results align with previous findings, further confirming the successful incorporation of Eu.

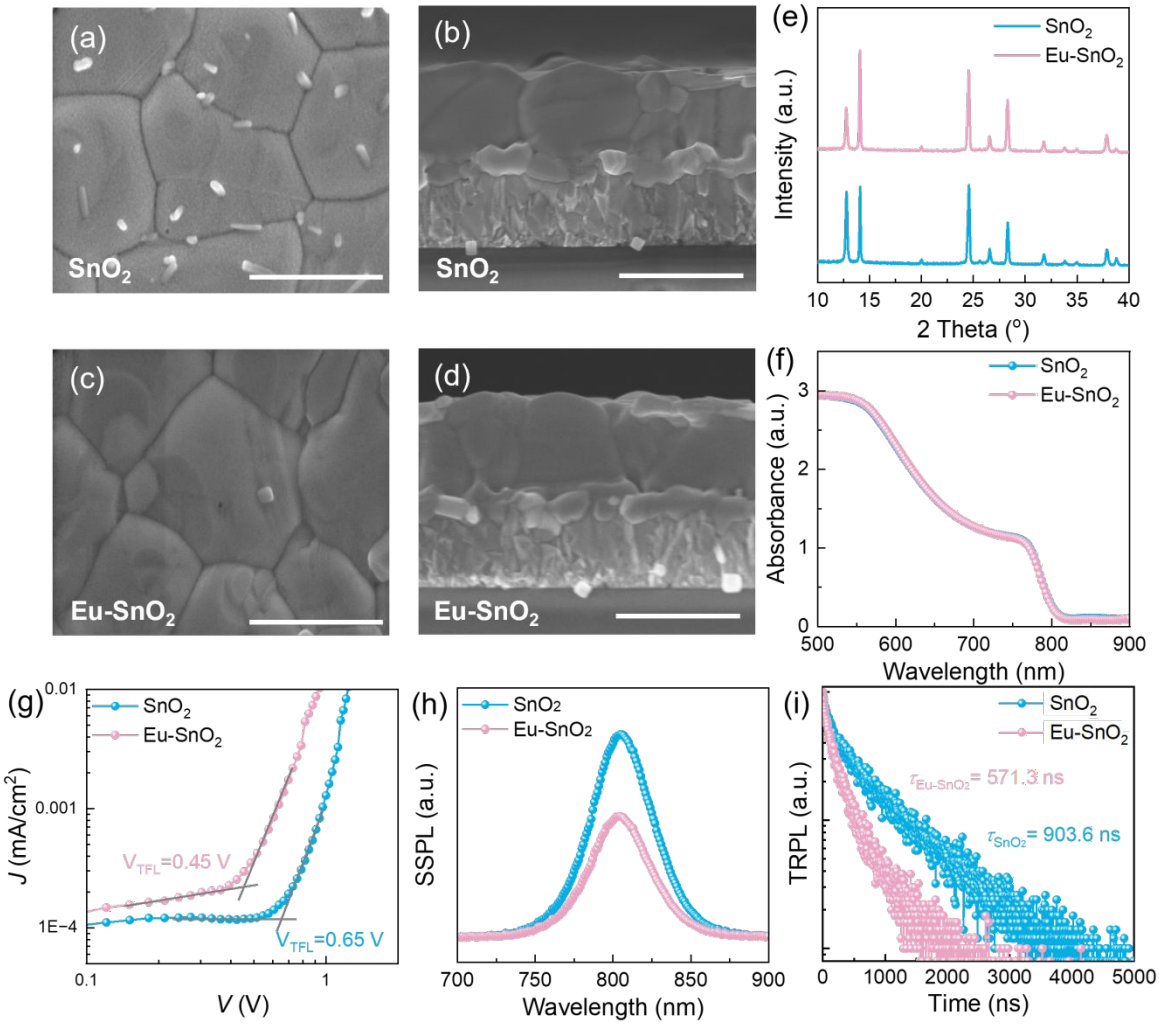

Fig. 3. (a) Top-view and (b) cross-sectional images of the perovskite film deposited on SnO_2 ETL. (c) Top-view and (d) cross-sectional images of perovskite film deposited on Eu-SnO_2 ETL. The scale bar is 1 μm. (e) XRD and (f) UV-vis spectra of perovskite films deposited on different ETL films. (g) Dark *J-V* curves of electron-only semi-devices with the structure FTO/ETL/perovskite/PCBM/Au. (h) SSPL spectra and (i) TRPL spectra of perovskite films deposited on different ETL substrates

To investigate the effect of Eu doping on the subsequent growth of perovskite, SEM was conducted to characterize the perovskite films, as shown in Fig. 3a-d. The surface morphologies of the perovskite films reveal large grain size and similar thickness (~850 nm thick) for both ETLs. However, the perovskite film on the SnO_2 ETL exhibits white clusters of lead compounds, which are absent in the perovskite film deposited on Eu-SnO_2, showing improved film quality. As shown in Fig. S7 (Supporting Information), energy dispersive spectrometer (EDS) analysis was performed to examine the distribution of Eu. The

View Article Online
DOI: 10.1039/D5SE01085F

results demonstrate that Eu ions diffuse into perovskite film during fabrication process, which is beneficial for enhancing the long-term stability of PSCs by eliminating the detrimental Pb^0 and I^0 defects within perovskite layers.[18] The corresponding X-ray diffraction (XRD) spectra are shown in Fig. 3e. The diffraction peak at 12.78° corresponds to the (001) plane of PbI_2, while the peaks at 14.07° and 24.57° correspond to the (100) and (111) planes of perovskite, respectively. Quantitative analysis of the peak area ratio of the PbI_2 (001) peak to the perovskite (100) peak shows a decrease from 1.41 for SnO_2 to 0.64 for Eu-SnO_2, indicating a lower PbI_2 content. Furthermore, Eu doping does not affect the transmittance of the ETL substrates, resulting in minimal impact on the light absorption of perovskite, as shown in Fig. 3f and Fig. S8 (Support Information).

The reduction in PbI_2 content suggests a decrease in trap defect densities in the perovskite film. To quantitatively assess the defect density, we fabricated an electron-only device with the structure FTO/SnO_2(or Eu-SnO_2)/perovskite/PCBM/Au using the space charge limiting current (SCLC) method. The defect density (N_{trap}) of the perovskite film can be calculated using the formula: $N_{trap}=2\varepsilon_0\varepsilon_r V_{TFL}/eL^2$, where ε_0 is the vacuum dielectric constant, ε_r is the relative dielectric constant of perovskite, e is the electron charge, L is the perovskite film thickness, and V_{TFL} is the voltage at which traps are filled. By fitting the SCLC spectra shown in Fig. 3g, the V_{TFL} decreased from 0.65 V for SnO_2 to 0.45 V for Eu-SnO_2. The calculated trap defect densities of perovskite films are 3.71×10^{15} cm^{-3} for SnO_2 ETL and 2.56×10^{15} cm^{-3} for Eu-SnO_2 ETL, respectively, indicating a reduction in trap density. To investigate the electron extraction efficiency and charge carrier recombination at the ETL/perovskite interface, we performed steady-state photoluminescence (SSPL) and time-resolved photoluminescence (TRPL) spectroscopy. As shown in Fig. 3h, the Eu-SnO_2-based perovskite film exhibits a lower SSPL intensity than the SnO_2-based sample, suggesting a stronger quenching effect and enhanced electron export ability. By fitting the TRPL curves shown in Fig. 3i with a double-exponential decay function,[30] the carrier lifetimes were determined to be 571.3 ns for SnO_2 and 903.6 ns for Eu-SnO_2, respectively. The shorter carrier lifetime for Eu-SnO_2 case indicates a faster charge extraction rate at the Eu-SnO_2/perovskite interface.

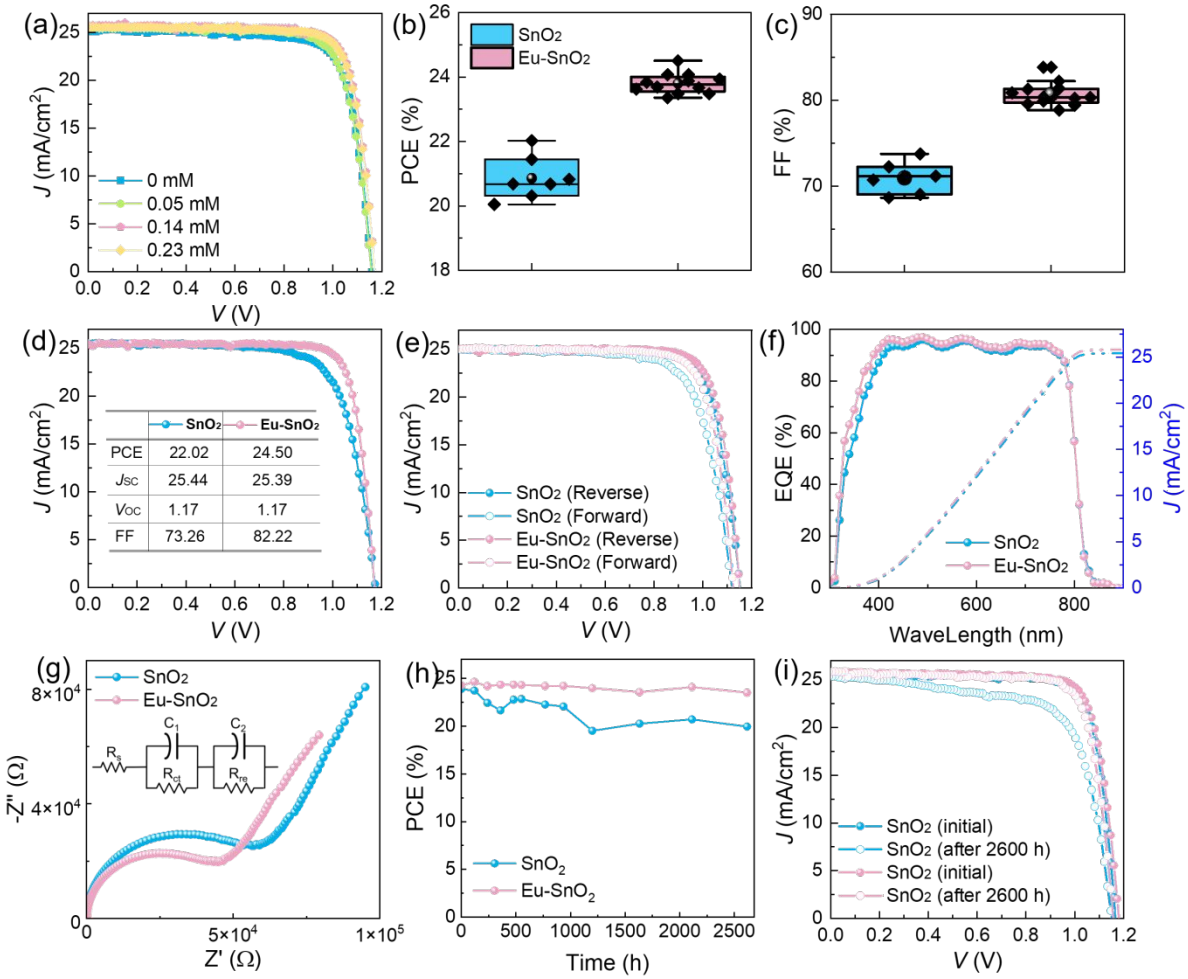

Fig. 4 (a) *J-V* curves of PSCs treated with different concentrations of $EuCl_3{\cdot}6H_2O$. Statistical (b) PCE and (c) FF of PSCs with different ETLs, including 7 SnO_2 samples and 11 Eu-SnO_2 samples. (d) Best-performing *J-V* curves of PSCs with different ETLs with an active area of 0.1 cm^2. (e) *J-V* curves of PSCs scanned at forward and reverse direction. (f) EQE and (g) EIS spectra of PSCs with different

View Article Online
DOI: 10.1039/D5SE00128E

ETLs. (h) Air-stability measurement of the PSCs stored in a drying closet with a humidity of 10±5%. (i) *J-V* curves of PSCs with different ETLs before and after aging.

To evaluate the effect of Eu doping on the photovoltaic performance of PSCs, we fabricated devices using SnO_2 and Eu-SnO_2 ETLs. The concentration of $EuCl_3{\cdot}6H_2O$ was optimized, with the *J-V* curves and corresponding photovoltaic parameters shown in Fig. 4a and Table S2, identifying 0.14 mM as the optimal. Fig. 4b, c and Fig. S9 (Supporting Information) present the statistical photovoltaic performance of PSCs based on these ETLs. The average PCE improved from 20.95% to 23.73%, primarily ascribed to the increase in fill factor (FF) from 71.28% to 80.55%. Fig. 4d displays the best-performing *J–V* curves for PSCs with different ETLs. The PCE of the device increased from 22.02% to 24.50% after Eu doping, benefiting from an improvement of FF from 73.26% to 82.22%. Additionally, the PSC with the Eu-SnO_2 ETL exhibits a much lower hysteresis index (HI) of 0.044 compared to 0.089 for the SnO_2-based device, as shown in Fig. 4e. Fig. 4f illustrates the external quantum efficiency (EQE) spectra of PSCs with different ETLs, showing integrated current density of 25.41 and 25.56 mA/cm^2, respectively, consistent with the short-circuit current density (J_{SC}) values from *J–V* measurements. The slight enhancement in the 300–400 nm range suggests improved charge charrier collection and transport efficiency. Electrochemical impedance spectroscopy (EIS) was conducted under dark condition at a bias voltage of 0.6 V to further investigate charge transport properties of PSCs with different ETLs, as shown in Fig. 4g. By fitting the EIS spectra, it is shown that the series resistance (R_s) of the PSC decreased from 19.44 Ω for SnO_2 to 16.08 Ω for Eu-SnO_2. Similarly, the charge transfer resistance (R_{tr}) dropped from 1.62 ×10^5 Ω to 4.60×10^4 Ω, indicating improved charge transfer efficiency due to Eu doping. Additionally, the charge recombination resistance (R_{rec}) increased from 5.87×10^4 Ω for the SnO_2-based device to 1.22×10^5 Ω for the Eu-SnO_2-based device, highlighting reduced non-radiative recombination at the buried interface. To check the influence of Eu doping on the stability of PSCs, the devices were stored in ambient air with a relative humidity (RH) of 10±5%. Fig. 4h recorded the efficiency evolution of PSCs based on different ETLs, while Fig. 4i and Table S7 present the corresponding *J-V* curves and photovoltaic parameters before and after 2600 h of storage. The aged PSC based on the Eu-SnO_2 ETL maintained 96.9% of its initial efficiency, while the SnO_2-based PSC degraded to 83.5%, demonstrating enhanced air-stability after Eu doping. Furthermore, we evaluated the UV stability of the device using a 100 W @365 nm UV light source in an N_2 filled glovebox, with a light intensity of 15 mW/cm^2. As shown in Fig. S10 (Support Information), after 130 h of UV irradiation, the Eu-SnO_2-based device retained 86% of its initial efficiency, while the SnO_2-based device maintained only 73%, showing the great potential of Eu in enhancing the light stability of PSCs. To give a deep investigation upon the degradation mechanism of PSCs, we conducted accelerated UV aging experiments on perovskite deposited on SnO_2 and Eu-SnO_2 films under UV illumination (light intensity: 130±10 mW/cm^2, wavelength: 395 nm) in an N_2 filled glovebox. After 50 h of irradiation, we carefully stripped off the perovskite and checked the buried perovskite interface.[31,32] The morphology changes before and after UV aging are showed in Fig. S11. In the pristine state, the perovskite fabricated with Eu-SnO_2 displayed reduced PbI_2 residue at grain boundaries compared to its SnO_2-based counterpart. Upon UV aging, the SnO_2-based samples underwent pronounced decomposition, evidenced by diminished grain sizes and the appearance of voids. Conversely, Eu-SnO_2-based perovskite maintained superior morphological stability, with a smoother surface and well-defined crystal grains. As shown in Fig. S12, the XRD patterns further corroborate these results. A quantitative assessment of perovskite degradation during aging was conducted by calculating the area ratio of the PbI_2 (001) diffraction peak relative to the combined areas of the perovskite (100), (111), and (220) diffraction peaks. The SnO_2-based sample exhibited a notable increase in this ratio from 22% to 49% following UV exposure, while the Eu-SnO_2-based counterpart showed only a marginal increase from 23% to 24%, highlighting its improved UV stability.

Conclusions

The quality of the SnO_2 ETL plays a decisive role in the photovoltaic performance of PSCs. In this work, Eu^{3+} ions were successfully incorporated into the SnO_2 lattice during the CBD process. The electrical properties of Eu-SnO_2, including conductivity and electron mobility, were significantly improved. Surface trap defects were effectively suppressed, facilitating more efficient charge carrier collection and transport at ETL/perovskite interface. More importantly, the incorporation of Eu^{3+} effectively mitigated UV-induced degradation in the perovskite films. As a result, the efficiency of the PSC increased from 22.02% to 24.50% after Eu doping. The devices also demonstrate excellent stability, maintaining 96.9% and 86% of their initial efficiency after 2600 h in ambient air and 130 h under continuous UV illumination, respectively. This work offers new insights for enhancing the efficiency and stability of PSCs.

Author contributions

M. Li conceived the project and edited the manuscript. D. Wu and H. Yan contributed equally to this work. D. Wu, X. Zhao designed the experiments and D. Wu performed the experiments. H. Yan, Y. Qiu, Y. Yang, Y. Zhang, B. Fan, P. Cui, X. Sun and P. Zhao assisted in testing and the data analysis. X. Zhao, H. Yan, D. Wu and M. Li contributed to the paper writing. All authors discussed and reviewed the manuscript.

Conflicts of interest

There are no conflicts to declare.

Data availability

Detailed experimental method, including materials, device fabrication, and film characterization, and additional experimental results and data are available in the ESI.

Acknowledgements

This work is supported partially by the Key Research and Development Program sponsored by the Ministry of Science and Technology (MOST) (Grant nos. 2022YFB4200301), National Natural Science Foundation of China (Grant nos. 22409061, 52232008, 51972110, 52102245, 52072121, and 52402254), Beijing Natural Science Foundation (2222076, 2222077), Beijing Nova Program (20220484016), Young Elite Scientists Sponsorship Program by CAST (2022QNRC001), 2022 Strategic Research Key Project of Science and Technology Commission of the Ministry of Education, Huaneng Group Headquarters Science and Technology Project (HNKJ20-H88), the Fundamental Research Funds for the Central Universities (2023MS042, 2023MS047) and the NCEPU "Double First-Class" Program.

Notes and references

1 H.-S. Kim, C.-R. Lee, J.-H. Im, K.-B. Lee, T. Moehl, A. Marchioro, S.-J. Moon, R. Humphry-Baker, J.-H. Yum, J. E. Moser, M. Grätzel and N.-G. Park, *Scientific Reports*, 2012, **2**, 591.
2 N. R. E. L. (NREL), Best Research-Cell Efficiencies, https://www.nrel.gov/pv/cell-efficiency.html.
3 L. Meng, J. You and Y. Yang, *Nature Communications*, 2018, **9**, 5265.
4 L. Zang, C. Zhao, X. Hu, J. Tao, S. Chen and J. Chu, *Small*, 2024, **20**, 2400807.
5 M. Haghighi, N. Ghazyani, S. Mahmoodpour, R. Keshtmand, A. Ghaffari, H. Luo, R. Mohammadpour, N. Taghavinia and M. Abdi-Jalebi, *Low-Temperature Processing Methods for Tin Oxide as Electron Transporting Layer in Scalable Perovskite Solar Cells*, 2023, vol. 7.
6 Q. Jiang, L. Zhang, H. Wang, X. Yang, J. Meng, H. Liu, Z. Yin, J. Wu, X. Zhang and J. You, *Nature Energy*, 2016, **2**, 16177.
7 E. H. Anaraki, A. Kermanpur, L. Steier, K. Domanski, T. Matsui, W. Tress, M. Saliba, A. Abate, M. Grätzel, A. Hagfeldt and J. P. Correa-Baena, *Energy and Environmental Science*, 2016, **9**, 3128–3134.
8 J. J. Yoo, G. Seo, M. R. Chua, T. G. Park, Y. Lu, F. Rotermund, Y. K. Kim, C. S. Moon, N. J. Jeon, J. P. Correa-Baena, V. Bulović, S. S. Shin, M. G. Bawendi and J. Seo, *Nature*, 2021, **590**, 587–593.
9 S. Y. Park and K. Zhu, *Advanced Materials*, 2022, **34**, 2110438.
10 J. Song, H. Liu, W. Pu, Y. Lu, Z. Si, Z. Zhang, Y. Ge, N. Li, H. Zhou, W. Xiao, L. Wang and M. Sui, *Energy and Environmental Science*, 2022, **15**, 4836–4849.
11 G. Tong, L. K. Ono, Y. Liu, H. Zhang, T. Bu and Y. Qi, *Nano-Micro Letters*, DOI:10.1007/s40820-021-00675-7.
12 H. Min, D. Y. Lee, J. Kim, G. Kim, K. S. Lee, J. Kim, M. J. Paik, Y. K. Kim, K. S. Kim, M. G. Kim, T. J. Shin and S. Il Seok, *Nature*, 2021, **598**, 444–450.
13 Z. Wu, J. Su, N. Chai, S. Cheng, X. Wang, Z. Zhang, X. Liu, H. Zhong, J. Yang, Z. Wang, J. Liu, X. Li and H. Lin, *Advanced Science*, 2023, **10**, 2300010.
14 J. H. Lee, S. J. Lee, T. Kim, H. Ahn, G. Y. Jang, K. H. Kim, Y. J. Cho, K. Zhang, J. S. Park and J. H. Park, *Joule*, 2023, **7**, 380–397.
15 J. Liang, X. Hu, C. Wang, C. Liang, C. Chen, M. Xiao, J. Li, C. Tao, G. Xing, R. Yu, W. Ke and G. Fang, *Joule*, 2022, **6**, 816–833.
16 R. Datt, S. Bishnoi, D. Hughes, P. Mahajan, A. Singh, R. Gupta, S. Arya, V. Gupta and W. C. Tsoi, *Solar RRL*, 2022, **6**, 2200266.
17 S. K. Jung, N. G. Park and J. W. Lee, *Materials Today Energy*, 2023, **37**, 101401.
18 L. Wang, H. Zhou, J. Hu, B. Huang, M. Sun, B. Dong, G. Zheng, Y. Huang, Y. Chen, L. Li, Z. Xu, N. Li, Z. Liu, Q. Chen, L.-D. Sun and C.-H. Yan, *Science*, 2019, **363**, 265–270.
19 Z. Song, W. Xu, Y. Wu, S. Liu, W. Bi, X. Chen and H. Song, *Small*, 2020, **16**, 2001770.
20 Y. Chen, X. Zuo, Y. He, F. Qian, S. Zuo, Y. Zhang, L. Liang, Z. Chen, K. Zhao, Z. Liu, J. Gou and S. F. Liu, *Advanced Science*, 2021, **8**, 2001466.
21 J. J. Yoo, G. Seo, M. R. Chua, T. G. Park, Y. Lu, F. Rotermund, Y. K. Kim, C. S. Moon, N. J. Jeon, J. P. Correa-Baena, V. Bulović, S. S. Shin, M. G. Bawendi and J. Seo, *Nature*, 2021, **590**, 587–593.
22 D. Kim, Y. H. Jin, K. W. Jeon, S. Kim, S. J. Kim, O. H. Han, D. K. Seo and J. C. Park, *RSC Advances*, 2015, **5**, 74790–74801.
23 C. Liu, J. Zhang, L. Zhang, X. Zhou, Y. Liu, X. Wang and B. Xu, *Advanced Energy Materials*, 2022, **12**, 2200945.
24 E. Malchukova and B. Boizot, *Mater. Res. Bull.*, 2010, **45**, 1299–1303.
25 P. K. Baitha and J. Manam, *Bull. Mater. Sci.*, 2016, **39**, 1233–1243.
26 Z. Lan, H. Huang, Y. Lu, S. Qu, M. Wang, S. Du, Y. Yang, C. Sun, Q. Zhang, Y. Suo, X. Wang, L. Yan, P. Cui, Z. Zhao and M. Li, *Advanced Functional Materials*, 2024, **34**, 2316591.
27 Y. Yang, H. Huang, L. Yan, P. Cui, Z. Lan, C. Sun, S. Du, X. Wang, C. Yao, S. Qu, Q. Zhang, M. Wang, X. Zhao and M. Li, *Advanced Energy Materials*, 2024, **14**, 2400416.
28 H. Kaur, H. S. Bhatti and K. Singh, *RSC Advances*, 2019, **9**, 37450–37466.
29 G. Singh, N. Kohli and R. C. Singh, *Journal of Materials Science: Materials in Electronics*, 2017, **28**, 2257–2266.
30 J. Chen, X. Zhao, S. G. Kim and N. G. Park, *Advanced Materials*, 2019, **31**, 1902902.
31 H.-S. Kim, C.-R. Lee, J.-H. Im, K.-B. Lee, T. Moehl, A. Marchioro, S.-J. Moon, R. Humphry-Baker, J.-H. Yum, J. E. Moser, M. Grätzel and N.-G. Park, *Sci. Rep.*, 2012, **2**, 591.
32 Y. Cao, X. Zhang, K. Zhao, Y. Wei, L. Zhang, H. Zhang, W. Wang, C. Cui, P. Wang, P. Lin, X. Wu, C. Song, Z. Ni, J. Xue, R. Wang and L. Xu, *Adv. Funct. Mater.*, 2025, 2422205.

View Article Online
DOI: 10.1039/D5SE00128E

Data availability

Detailed experimental method, including materials, device fabrication, and film characterization, and additional experimental results and data are available in the ESI.